Article

Versatile Interplay of Chalcogenide and Dichalcogenide Anions in the Thiovanadate $Ba_7S(VS_3O)_2(S_2)_3$ and Its Selenide Derivatives: Elaboration and DFT Meta-GGA Study

Batoul Almoussawi, Hiroshi Kageyama, Pascal Roussel, and Houria Kabbour*

Cite This: ACS Org. Inorg. Au 2023, 3, 158−170

Read Online

ACCESS | Metrics & More | Article Recommendations | SI Supporting Information

ABSTRACT: Oxychalcogenides are emerging as promising alternative candidates for a variety of applications including for energy. Only few phases among them show the presence of Q−Q bonds (Q = chalcogenide anion) while they drastically alter the electronic structure and allow further structural flexibility. Four original oxy(poly)chalcogenide compounds in the system Ba−V−Q−O (Q = S, Se) were synthesized, characterized, and studied using density functional theory (DFT). The new structure type found for $Ba_7V_2O_2S_{13}$, which can be written as $Ba_7S(VS_3O)_2(S_2)_3$, was substituted to yield three selenide derivatives $Ba_7V_2O_2S_{9.304}Se_{3.696}$, $Ba_7V_2O_2S_{7.15}Se_{5.85}$, and $Ba_7V_2O_2S_{6.85}Se_{6.15}$. They represent original multiple-anion lattices and first members in the system Ba−V−Se−S−O. They exhibit in the first layer heteroleptic tetrahedra $V^{5+}S_3O$ and isolated Q^{2-} anions and in the second layer dichalcogenide pairs $(Q_2)^{2-}$ with Q = S or Se. Selenide derivatives were attempted by targeting the selective substitution of isolated Q^{2-} or $(Q_2)^{2-}$ (in distinct layers) or both by selenide, but it systematically led to concomitant and partial substitution of both sites. A DFT meta-GGA study showed that selective substitution yields local constraints due to rigid VO_3S and pairs. Experimentally, incorporation of selenide in both layers avoids geometrical mismatch and constraints. In such systems, we show that the interplay between the O/S anionic ratio around V^{5+}, together with the presence/nature of the dichalcogenides $(Q_2)^{2-}$ and isolated Q^{2-}, impacts in unique manners the band gap and provides a rich background to tune the band gap and the symmetry.

KEYWORDS: oxychalcogenides, dichalcogenide pairs, band-gap engineering, DFT, thiovanadates
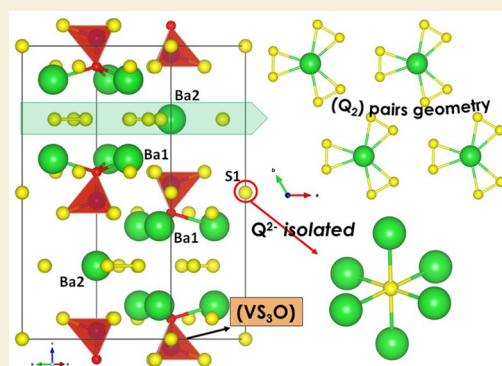
INTRODUCTION

Oxychalcogenides are, among mixed-anion compounds,[1] growing in popularity because of their great versatility and tunable properties for a large scope of applications. They open new perspectives to overcome challenges and hindrances to the development of various applications such as thermoelectrics[2,3] or photocatalytic hydrogen production,[4,5] and so on. The coexistence of oxide anions and more electronegative chalcogenide anions Q (Q = chalcogenide) leads to a highly distinctive structural chemistry.[6]

In this context, many oxychalcogenide compounds exhibit 2D layered-type structures, such as the narrow band-gap semiconductors $Sr_2CuO_2Cu_2Se_2$,[7] $Bi_2YO_4Cu_2Se_2$,[8] or the superconductors $LaO_{1-x}F_xBiS_2$.[9] Besides, few complex oxychalcogenides show the presence of Q−Q bonds (Q = chalcogenide anion) leading to polychalcogenide anions, which drastically affects the electronic structure and therefore the physical properties.[10] Some "simple" binaries such as cobalt persulfide CoS_2[11] or perselenide $CoSe_2$[12] are well-known dichalcogenide anion-based compounds. They are widely studied for their catalytic properties.[13] Polychalcogenides are also crucial in lithium−sulfur batteries, which are among the

most promising technologies in this field.[14] Recently, new compounds could be designed by a redox metal insertion into polychalcogenide-based phases.[10,15] While polychalcogenide anions show great diversity, fewer complex inorganic systems containing them are found. The latter may show, for instance, very interesting features to enhance thermoelectric properties such as in $BaBiTe_{3-x}Se_x$[16] or $A_2BaCu_8Te_{10}$ (A = K, Rb, Cs).[17] Besides, oxychalcogenides with polychalcogenide anions are limited. $La_2O_2S_2$ and its derivatives are well-known materials for optics and are made of layers of La_2O_2 stacked with a layer of disulfide pairs.[18] Recently, topochemical (de)intercalation of sulfur in the latter was demonstrated, which opened new perspectives.[19] On the other hand, we recently reported the phase $Ba_5(VO_2S_2)_2(S_2)_2$[20] that contains dichalcogenide pairs
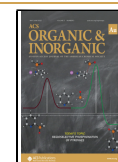
Table 1. Data Collection and Refinement Details of $Ba_7V_2O_2S_{13}$ and Its Selenide Derivatives (Phase 1 → 4)

	phase 1	phase 2	phase 3	phase 4
formula	$Ba_7V_2O_2S_{13}$	$Ba_7V_2O_2S_{9.304}Se_{3.696}$	$Ba_7V_2O_2S_{7.15}Se_{5.85}$	$Ba_7V_2O_2S_{6.85}Se_{6.15}$
detailed formula	$Ba_7S(VS_3O)_2(S_2)_3$	$Ba_7S_{1-\alpha}Se_\alpha(VS_3O)_2(S_{1-\delta}Se_\delta)_6$	$Ba_7S_{1-\alpha}Se_\alpha(VS_3O)_2(S_{1-\delta}Se_\delta)_6$	$Ba_7S_{1-\alpha}Se_\alpha(VS_3O)_2(S_{1-\delta}Se_\delta)_6$
α	0	0.496	0.790	0.903
δ	0	0.533	0.843	0.875
molecular weight (g·mol^{-1})	1512	1694.5	1786.4	1800.5
symmetry	hexagonal	hexagonal	hexagonal	hexagonal
space group	$P6_3/m$ (176)	$P6_3/m$ (176)	$P6_3/m$ (176)	$P6_3/m$ (176)
unit cell dimensions (Å)	$a = 8.8456(4)$	$a = 8.9290(3)$	$a = 8.9670(3)$	$a = 8.9706(2)$
	$c = 17.3971(8)$	$c = 17.6052(5)$	$c = 17.6747(7)$	$c = 17.6964(5)$
volume (Å^3)	1178.86(9)	1215.56(7)	1230.77(8)	1233.27 (5)
Z	2	2	2	2
Data Collection				
equipment	Bruker CCD (Mo Kα)	Bruker CCD (Mo Kα)	Bruker CCD (Mo Kα)	Bruker CCD (Ag Kα)
Λ [Å]	0.71073	0.71073	0.71073	0.56087
calculated density (g·cm^{-3})	4.2597	4.6295	4.8204	4.8841
crystal shape	platelet	platelet	platelet	platelet
crystal dimensions (μm)	$75 \times 50 \times 5$	$50 \times 30 \times 5$	$80 \times 45 \times 5$	$150 \times 50 \times 6$
color	dark	dark	dark	dark
absorption correction	multiscan	multiscan	multiscan	multiscan
scan mode	ω, ϕ	ω, ϕ	ω, ϕ	ω, ϕ
θ (min − max) (deg)	2.34−27.88	2.31−28.7	2.3−41.16	1.82−25.26
μ (mm^{-1})	13.391	18.477	20.981	11.277
F(000)	1324	1464	1535	1545
reciprocal space recording	$-11 \leq h \leq 11$	$-12 \leq h \leq 12$	$-16 \leq h \leq 16$	$-13 \leq h \leq 13$
	$-11 \leq k \leq 11$	$-11 \leq k \leq 12$	$-16 \leq k \leq 16$	$-13 \leq k \leq 13$
	$-22 \leq l \leq 22$	$-23 \leq l \leq 23$	$-32 \leq l \leq 32$	$-26 \leq l \leq 26$
no. of measured reflections	18823	23554	87170	62907
no. of independent reflections	979	1084	2813	1540
$I > 3\sigma(I)$ (total)	671	876	2044	1292
Refinement				
number of refined parameters	41	42	43	43
refinement method	least-squares	least-squares	least-squares	least-squares
weighting scheme	sigma	sigma	sigma	sigma
$R_1(F)$ $[I > 3\sigma(I)]/R_1(F^2)$ (all data, %)	0.0287/0.0551	0.0191/0.027	0.024/0.039	0.0404/0.0551
$wR_2(F^2)$ $[I > 3\sigma(I)]/wR_2(F^2)$ (all data, %)	0.0648/0.0720	0.0506/0.0517	0.0598/0.0627	0.0591/0.0612
goodness of fit	1.05	1.28	1.21	3.26
max/min residual electronic density (e$^-$/Å^3)	2.49/−1.56	2.47/−1.74	1.05/−1.78	3.66/−2.71
T_{min}/T_{max}	0.629/746	0.564/0.746	0.568/0.748	0.660/0.740

occupying in a unique 1D manner channels delimited by barium cations. This compound was the first in the Ba−V−S−O system with persulfide entities, while the conventional following oxysulfides were reported: $Ba_6V_4O_5S_{11}$,[21] $Ba_3V_2S_4O_3$,[22] $Ba_{15}V_{12}S_{34}O_3$,[23] and $Ba_{10}S(VO_3S)_6$.[24] All of these compounds exhibit tetrahedral thiovanadates as found in the simple series $A_3(VO_{4-x}S_x)$[25] (A = Na, K) with disconnected VO_2S_2 in the case of $Ba_5(VO_2S_2)_2(S_2)_2$.

In this work, we present four new complex polychalcogenide phases. The new phase $Ba_7S(VS_3O)_2(S_2)_3$ (phase 1) contains VS_3O thiovanadates and isolated S^{2-} anions into a layer and an original arrangement of persulfide $(S_2)^{2-}$ pairs into the second layer, thus leading to a complex anionic interplay. This is amplified in the three selenide derivatives $Ba_7V_2O_2S_{9.304}Se_{3.696}$, $Ba_7V_2O_2S_{7.15}Se_{5.85}$, and $Ba_7V_2O_2S_{6.85}Se_{6.15}$, which exhibit five anionic species (O^{2-}, S^{2-}, Se^{2-}, $(S_2)^{2-}$, and $(Se_2)^{2-}$). For all phases, a comparative crystallochemical discussion based on single-crystal XRD is complemented by electronic structure analysis calculated from density functional theory together with

optical properties of high-purity powder samples. We show multiple possibilities and complex anionic interplay in this system and carry out a comprehensive study.

■ EXPERIMENTAL SECTION

Synthesis

The powders were obtained from a mixture of 2BaO, 5BaS, 2V, and 8S pressed into pellets and heated in an evacuated sealed quartz tube. The heat treatment consisted in heating up to 750 °C for 24 h, then cooling down to 650 °C at a 5 °C/h rate, and finishing with a rapid cooling down to room temperature.

Initially, $Ba_7V_2O_2S_{13}$ was found in a preparation obtained at high pressure, which is described in the Supporting Information. It has a similar structure with a slightly decreased volume due to the preparation conditions. This phase could then be obtained in a sealed quartz tube as described above.

Table 2. Atomic Positions and Isotropic Thermal Displacement for $Ba_7O_2S_{13}V_2$ and the Selenide Derivatives

atom	Wyck.		x	y	z	U_{eq}
			$Ba_7S(VS_3O)_2(S_2)_3$			
Ba1	2d		0.666667	0.333333	0.25	0.0180(3)
Ba2	12i		0.0865(1)	0.3307(1)	0.1148(1)	0.0159(2)
S1	2b		0	0	0	0.0225(14)
S2	6h		0.2456 (4)	0.1899(4)	0.25	0.0165(11)
S3	6h		0.3861(4)	0.4669(3)	0.25	0.0163(11)
V1	4f		0.333333	0.666667	−0.0278(1)	0.0127(6)
S4	12i		0.5628(3)	0.6745(3)	−0.0703(1)	0.0202(8)
O1	4f		0.33333	0.66667	0.0690(2)	0.014(2)
			$Ba_7V_2O_2S_{9.304}Se_{3.696}$			
Ba1	12i		0.6659(1)	0.9117(1)	0.61254(1)	0.0169(1)
Ba2	2c		0.333333	0.666667	0.25	0.0191(2)
Se1	2b	0.496	0	0	0	0.0161(4)
S1	2b	0.504	0	0	0	0.0161(4)
Se2	6h	0.533	0.1794(1)	0.2365(1)	0.25	0.0148(3)
S2	6h	0.467	0.1794(1)	0.2365(1)	0.25	0.0148(3)
Se3	6h	0.533	0.4801(1)	0.3899(1)	0.25	0.0187(3)
S3	6h	0.467	0.4801(1)	0.3899(1)	0.25	0.0187(3)
V1	4f		0.33333	0.66667	0.47120(6)	0.0147(3)
S4	12i		0.1145(1)	0.6760(1)	0.4293(1)	0.0246(5)
O1	4f		0.33333	0.66667	0.5670(2)	0.0116(12)
			$Ba_7V_2O_2S_{7.15}Se_{5.85}$			
Ba1	12i		0.6656(1)	0.9116(2)	0.6111(1)	0.0148(1)
Ba2	2c		0.33333	0.66667	0.25	0.0192(1)
Se1	2b	0.790	0	0	0	0.0142(1)
S1	2b	0.21	0	0	0	0.0142(1)
Se2	6h	0.843	0.0583(1)	0.8233(1)	0.25	0.0145(1)
S2	6h	0.157	0.0583(1)	0.8233(1)	0.25	0.0145(1)
Se3	6h	0.843	0.6091(1)	0.0927(1)	0.25	0.0158(1)
S3	6h	0.157	0.6091(1)	0.0927(1)	0.25	0.0158(1)
V1	4f		0.33333	0.66667	0.4708(1)	0.0134(1)
S4	12i		0.1145(1)	0.6754(1)	0.4289(1)	0.0217(2)
O1	4f		0.33333	0.66667	0.5664(1)	0.0129(6)
			$Ba_7V_2O_2S_{6.85}Se_{6.15}$			
Ba1	12i		0.2472(1)	0.9124(1)	0.6113(1)	0.0114(2)
Ba2	2c		0.33333	0.66667	0.25	0.0169(3)
Se1	2b	0.9028	0	0	0	0.0151(6)
S1	2b	0.0972	0	0	0	0.0151(6)
Se2	6h	0.875	0.0580(2)	0.2347(2)	0.25	0.0109(5)
S2	6h	0.125	0.0580(2)	0.2347(2)	0.25	0.0109(5)
Se3	6h	0.875	0.4837(2)	0.0931(2)	0.25	0.0122(5)
S3	6h	0.125	0.4837(2)	0.0931(2)	0.25	0.0122(5)
V1	4f		0.33333	0.66667	0.4704(1)	0.0089(6)
S4	12i		0.3250(3)	0.8862(3)	0.4289(1)	0.0146(8)
O1	4f		0.33333	0.66667	0.5671(5)	0.010(2)

X-ray Diffraction

X-ray diffraction on single crystals for $Ba_7V_2O_2S_{13}$ and the selenide derivatives was performed on an X8 diffractometer equipped with a two-dimensional (2D) CCD 4K detector and an Ag Kα.

Powder XRD

The powder XRD patterns were collected on a Bruker D8 diffractometer equipped with a Lynxeye linear detector (Cu Kα) in Bragg−Brentano geometry at room temperature.

Scanning Electron Microscopy (SEM)

SEM experiments and EDX analysis were carried out on an S-3400N (Oxford instruments) and on a Hitachi S400N microscope.

DFT Calculations

DFT calculations were carried out by employing the projector augmented wave (PAW)[26,27] method encoded in the Vienna ab initio simulation package (VASP)[28] and the meta-GGA SCAN functional[29,30] for the exchange-correlation functionals. The full geometry optimizations were carried out using a plane-wave energy cutoff of 550 eV and 30 k points in the irreducible Brillouin zone for all models. It converged with residual Hellman−Feynman forces on the atoms smaller than 0.03 eV/Å and led to a good match with the experimental structure, i.e., within a reasonable error expected for the SCAN meta-GGA functional, which led in general to a better match with experience than simple GGA functionals. The relaxed structure was used for calculations of the electronic structure for which a plane-wave cutoff energy of 550 eV and threshold of self-consistent-field energy convergence of 10^{-6} eV were used, with 72 k points in the irreducible Brillouin zone for all models.

Table 3. Anisotropic Thermal Parameters U_{ij} (Å^2) for the Sulfide and the Selenide Derivatives

atom	U_{11}	U_{22}	U_{33}	U_{12}	U_{13}	U_{23}
			$Ba_7S(VS_3O)_2(S_2)_3$			
Ba1	0.0151(4)	0.0151(4)	0.0237(6)	0.0076(2)	0	0
Ba2	0.0136(4)	0.0173(2)	0.0164 (2)	0.0074(2)	0.0009(2)	0.0033(2)
S1	0.0173(15)	0.0173(15)	0.033(3)	0.0087(8)	0	0
S2	0.0177(13)	0.0162(14)	0.0168(13)	0.0093(12)	0	0
S3	0.0169(14)	0.0158(14)	0.0152(12)	0.0074(11)	0	0
V1	0.0146(7)	0.0146(7)	0.0089(10)	0.0073(3)	0	0
S4	0.0179(10)	0.0198(10)	0.0231(10)	0.0095(9)	0.0049(8)	0.0019(8)
O1	0.018(3)	0.018(3)	0.004(4)	0.0092(14)	0	0
			$Ba_7V_2O_2S_{9.304}Se_{3.696}$			
Ba1	0.0174(1)	0.0147(1)	0.0173(1)	0.0071(1)	−0.0032(1)	−0.0009(1)
Ba2	0.0153(2)	0.0153(2)	0.0269(3)	0.0076(1)	0	0
Se1	0.0150(5)	0.0150(5)	0.0182(8)	0.0075(3)	0	0
S1	0.0150(5)	0.0150(5)	0.0182(8)	0.0075(3)	0	0
Se2	0.0149(4)	0.0174(4)	0.0137(4)	0.0092(4)	0	0
S2	0.0149(4)	0.0174(4)	0.0137(4)	0.0092(4)	0	0
Se3	0.0185(4)	0.0181(5)	0.0181(4)	0.0081(4)	0	0
S3	0.0185(4)	0.0181(5)	0.0181(4)	0.0081(4)	0	0
V1	0.0171(4)	0.0171(4)	0.0099(5)	0.0085(2)	0	0
S4	0.0238(6)	0.0250(6)	0.0286(6)	0.0152(6)	−0.0061(4)	0.0004(5)
O1	0.0128(14)	0.0128(14)	0.009(2)	0.0064(7)	0	0
			$Ba_7V_2O_2S_{7.15}Se_{5.85}$			
Ba1	0.0149(1)	0.0139(1)	0.0148(1)	0.0065(1)	−0.0013(1)	−0.0006(1)
Ba2	0.0147(1)	0.0147(1)	0.0281(2)	0.0073(1)	0	0
Se1	0.0136(2)	0.0136(2)	0.0155(3)	0.0068(1)	0	0
S1	0.0136(2)	0.0136(2)	0.0155(3)	0.0068(1)	0	0
Se2	0.0141(1)	0.0137(1)	0.0144(1)	0.0060(1)	0	0
S2	0.0141(1)	0.0137(1)	0.0144(1)	0.0060(1)	0	0
Se3	0.0160(1)	0.0174(2)	0.0155(2)	0.0094(1)	0	0
S3	0.0160(1)	0.0174(2)	0.0155(2)	0.0094(1)	0	0
V1	0.0157(2)	0.0157(2)	0.0090(2)	0.0078(1)	0	0
S4	0.0210(3)	0.0223(3)	0.0247(3)	0.0130(2)	−0.0057(2)	0.0006(2)
O1	0.0152(7)	0.0152(7)	0.0082(10)	0.0076(3)	0	0
			$Ba_7V_2O_2S_{6.85}Se_{6.15}$			
Ba1	0.0114(3)	0.0099(3)	0.0119(3)	0.0046(2)	0.0007(2)	−0.0005(2)
Ba2	0.0120(4)	0.0120(4)	0.0267(7)	0.0060(2)	0	0
Se1	0.0139(7)	0.0139(7)	0.0175(10)	0.0069(3)	0	0
S1	0.0139(7)	0.0139(7)	0.0175(10)	0.0069(3)	0	0
Se2	0.0110(6)	0.0124(6)	0.0101(6)	0.0064(5)	0	0
S2	0.0110(6)	0.0124(6)	0.0101(6)	0.0064(5)	0	0
Se3	0.0118(6)	0.0145(7)	0.0104(6)	0.0067(5)	0	0
S3	0.0118(6)	0.0145(7)	0.0104(6)	0.0067(5)	0	0
V1	0.0084(7)	0.0084(7)	0.0099(10)	0.0042(3)	0	0
S4	0.0153(10)	0.0115(10)	0.0183(10)	0.0078(9)	−0.0007(9)	0.0039(8)
O1	0.013(3)	0.013(3)	0.004(4)	0.0065(15)	0	0

UV−Visible Measurements

The reflectance of the sample was measured from 250 to 800 nm on a PerkinElmer Lambda 650 device.

■ RESULTS AND DISCUSSION

Structure Resolution and Description

$Ba_7S(VS_3O)_2(S_2)_3$. A dark single crystal with a platelet shape was selected for XRD data collection. The structure could be solved with the unit cell parameters a = 8.8172(4) Å and c = 17.3428(8) Å in the space group $P6_3/m$ (176). The data collection, refinement details, and structural parameters are given in Tables 1−4. The refinement was carried out with JANA2006[31] software based on a structure solution obtained with the charge-flipping method implemented in JANA2006

within the SUPERFLIP module.[32] EDX analysis of the single crystals led to the average atomic ratio 59.53/8.70/31.77 for S/V/Ba, respectively, in good agreement with the formula $Ba_7V_2O_2S_{13}$.

The original structure can be viewed as a rather open framework but can be described by two alternating layers (Figure 1d). The first layer is formed by disconnected VS$_3$O tetrahedra (Figure 1a) separated from each other by Ba^{2+} cations that also coordinate isolated sulfide S$^{2−}$ (S1) anions into the S1Ba$_6$ octahedron with $d_{Ba1−S1}$= 3.282(2) Å; this distance is typical of a Ba^{2+}−S$^{2−}$ bond and is, for instance, comparable to that found in $Ba_9V_3S_{11}(S_2)_2$,[33] $d_{Ba−S}$ = 3.173(2) Å (see Figure 1c). In the mixed-anion tetrahedra based on V^{5+}, we found V1−S4 = 2.121(1) Å (×3) and V1−O1 = 1.688(3)

Table 4. Main Distances (Å) for $Ba_7O_2S_{13}V_2$ and the Selenide Derivatives

atoms 1 and 2	d 1 and 2 [Å]	atoms 1 and 2	d 1 and 2 [Å]
	$Ba_7S(VS_3O)_2(S_2)_3$		
Ba1–S2	3.280(3) × 3	Ba2–S4	3.220(3)
Ba1–S3	3.238(4) × 3	Ba2–S4	3.251(2)
Ba2–S1	3.3002(5)	Ba2–O1	2.783(2)
Ba2–S2	3.289(2)	V1–O1	1.684(2)
Ba2–S3	3.289(3)	V1–S4	2.129(2) × 3
Ba2–S4	3.3309(19)	S2–S3	2.122(4)
	$Ba_7V_2O_2S_{9.304}Se_{3.696}$		
Ba1–Se1	3.3308(3)	Ba1–O1	2.7842(11)
Ba1–Se2	3.3678(8)	Ba2–Se2	3.3709(9) × 3
Ba1–Se2	3.4313(6)	Ba2–Se3	3.3261(10) × 3
Ba1–Se3	3.3611(6)	V1–O1	1.687(4)
Ba1–S4	3.2744(15)	V1–S4	2.129(2) × 3
Ba1–S4	3.257(2)	Se2–Se3	2.3253(16)
	$Ba_7V_2O_2S_{7.15}Se_{5.85}$		
Ba1–Se1	3.3310(8)	Ba1–O1	2.7891(10)
Ba1–Se2	3.4075(5)	Ba2–Se2	3.3944(6) × 3
Ba1–Se3	3.3981(4)	Ba2–Se3	3.3552(5) × 3
Ba1–S4	3.3310(8)	V1–O1	1.692(4)
Ba1–S4	3.2855(8)	V1–S4	2.1364(7)
Ba1–S4	3.2664(12)	Se2–Se3	2.3832(4)
	$Ba_7V_2O_2S_{6.85}Se_{6.15}$		
Ba1–Se1	3.3400(7)	Ba1–O1	2.788(3)
Ba1–Se2	3.4136(12)	Ba2–Se2	3.398(1) × 3
Ba1–Se3	3.4015(16)	Ba2–Se3	3.360(3) × 3
Ba1–S4	3.335(2)	V1–O1	1.711(9)
Ba1–S4	3.286(2)	V1–S4	2.138(3) × 3
Ba1–S4	3.274(2)	Se2–Se3	2.385(3)

Å. These distances are comparable to those found, for instance, in thiovanadates within $Ba_5V_2S_8O_4$ (Figure 1h), i.e., V1–S1 =

2.178(2) Å and V1–O2 = 1.680(5) Å, or in $Ba_{15}V_{12}S_{34}O_3$ with comparable distances. The polar $[VS_3O]^{3-}$ tetrahedral entities are arranged with their O vertices along the crystallographic unique axis c, but the space group inversion symmetry makes them alternatively point in the opposite direction along c so that no polar arrangement arises from them (Figure 1e), in contrast to $K_3(VO_3S)$[34] for instance. The second layer consists of disulfide pairs $(S_2)^{2-}$ surrounded by Ba^{2+} cations (Figure 1g). These Ba^{2+} cations are distributed such as forming cavities. In the latter, the disulfide pairs are arranged pointing in three different directions. Three distinct pairs (representing the three different orientations) coordinate Ba2. Such an arrangement of disulfide pairs is original to the best of our knowledge. The two layers forming the structure are linked via weak Ba1–O1 (Figure 1b,1f) bonds. $Ba_7V_2S_{13}O_2$ can be written as $Ba_7(S_2)_3(VS_3O)_2S$ to consider the structural units involved.

Investigating Selective Substitution of Sulfur by Selenium

Starting from $Ba_7S(S_2)_3(VS_3O)_2$, we have attempted selective substitution by selenide anions. We targeted either the (Q_2) sites or the isolated Q^{2-} site or both, in $Ba_7(Q^{2-})-(VS_3O)_2(Q_2)_3$. We present here the results fulfilled for three compositions. In the high-purity powders obtained for the targeted substitutions $Ba_7S(VS_3O)_2(Se_2)_3$ (i.e., $Ba_7V_2O_2S_7Se_6$) and $Ba_7Se(VS_3O)_2(Se_2)_3$ (i.e., $Ba_7V_2O_2S_6Se_7$), single crystals were found. They correspond to similar structures as the parent phase. They show the average refined compositions of $Ba_7V_2O_2S_{7.15}Se_{5.85}$ and $Ba_7V_2O_2S_{6.85}Se_{6.15}$, i.e., close to the nominal ones, but the refinements (which will be further detailed below) show a disordered distribution of Se in both Q^{2-} and (Q_2) sites (VS_3O is not altered) with mixed S/Se sites. Then, $Ba_7S(VS_3O)_2(SeS)_3$ (i.e., $Ba_7V_2O_2S_{10}Se_3$) was attempted to lower the Se content and force a selective substitution in Q_2. In the corresponding preparation, a single
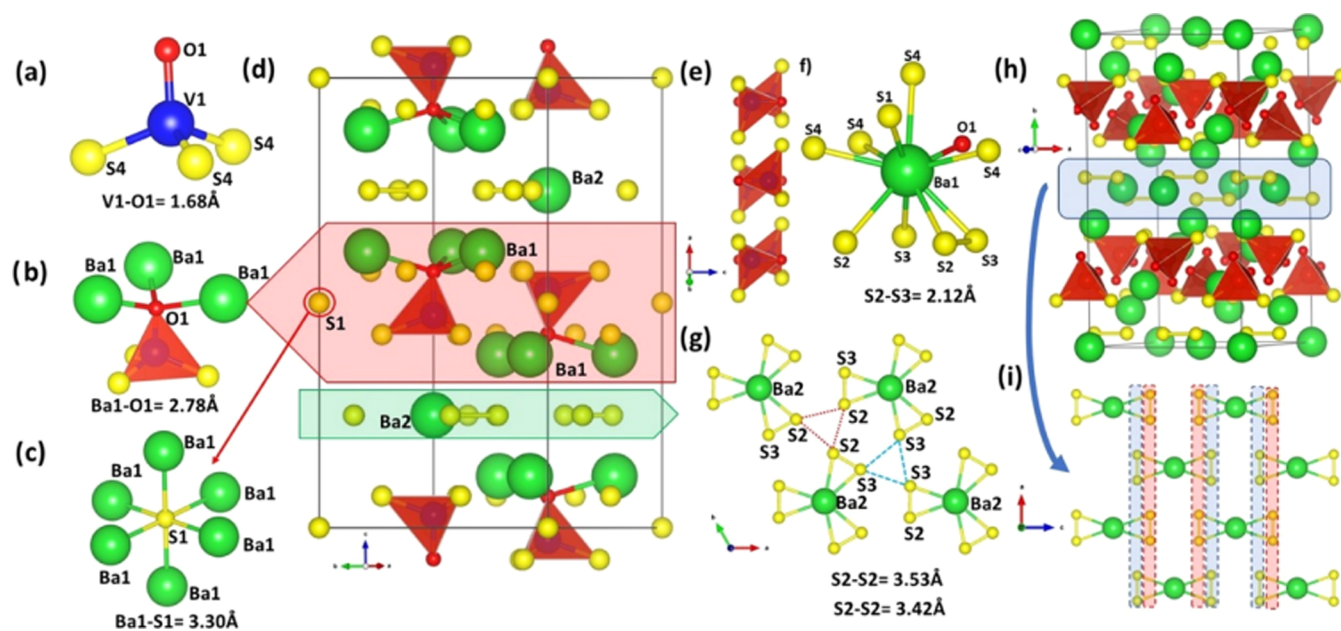

Figure 1. (a) View of the heteroleptic entity VS_3O with the V1–O1 distance indicated, (b) O1 atom environments with Ba–O1 distance, and (c) S1 atom environments with S1–Ba1 distance indicated. (d) Structure of $Ba_7V_2S_{13}O_2$. (e) View of the tetrahedra arrangement projected along the deviated b axis, (f) Ba1 environments with S2–S3 bonds and distances indicated, and (g) S2–S3 bonds arrangement represented around Ba2; the dotted lines represent the separations S2–S2 and S3–S3 (unconnected atoms). (h) View of $Ba_5(VO_2S_2)_2(S_2)_2$ (ref 20) and its (i) disulfide pair rearrangement.
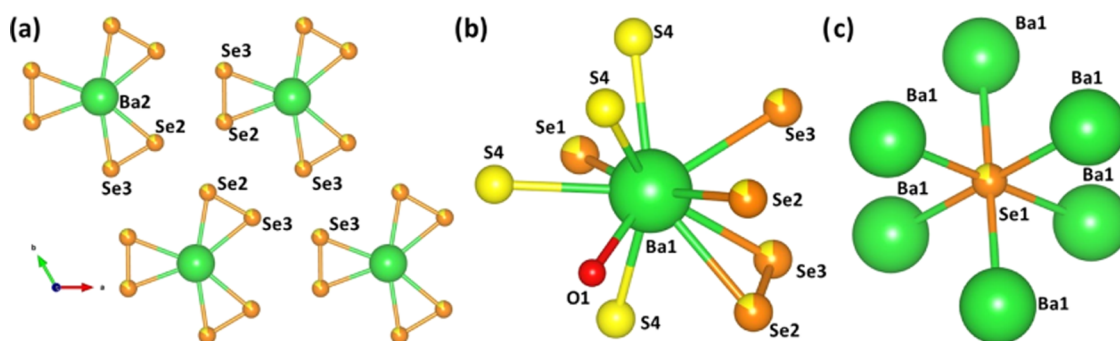
Figure 2. (a) Se2−Se3 bond arrangement represented when present in their vicinity: Ba2 and its connectivity with Se2−Se3 bonds. (b) Ba1 environments. (c) Isolated Se1 atom environment. To simplify, the mixed sites Se1/S1 are designed by Se1 and so on for Se2 and Se3.

Table 5. Main Geometrical Information for Phases 1, 2, 3, and 4 from the Single-Crystal Refinements

	phase 1	phase 2	phase 3	phase 4
unit cell parameters, Å	$a = 8.8456(4)$, $c = 17.3971(8)$	$a = 8.9290(3)$, $c = 17.6052(5)$	$a = 8.9670(3)$, $c = 17.6747(7)$	$a = 8.9706(2)$, $c = 17.6964(5)$
volume, Å^3	1178.86(9)	1215.56(7)	1230.77(8)	1233.27 (7)
VO_3S (Td) distances (Å)	V−O = 1.683(7)	V−O = 1.687(4)	V−O = 1.689(2)	V−O = 1.711(9)
	V−S = 2.129(3)	V−S = 2.129(2)	V−S = 2.1355(8)	V−S = 2.138(2)
Ch−Ch (Å)	2.122(6) (S_2)	2.325(1)	2.3832(4)	2.385(3)
Ba1−Ch$_{(isolé)}$	3.3002(5)	3.3308(3)	3.3323(2)	3.340(1)
Ba2−Ch$_{(paire)}$	3.289(2)	3.3259(9)/3.3712(7)	3.3940(3)/3.3557(4)	3.3978(1)/3.360(2)
Ba2−S4 interlayer	3.709(2)	3.736(1)	3.74258(7)	3.748(1)
band gap (eV)	1.59	1.53	1.51	1.49

crystal was selected and its structure resolution revealed also a composition close ($Ba_7V_2O_2S_{9.304}Se_{3.696}$) to the nominal one but again with the disordered incorporation of selenide in both $Q/(Q_2)$. The disordered dichalcogenide pairs in the selenide derivatives are arranged (Figure 2a) in the same manner as the disulfide pairs in the oxysulfide parent. Considering the single crystals found in the three above-mentioned preparations, we thus have characterized, in addition to $Ba_7S(VS_3O)_2(S_2)_3$, the following three selenide derivatives: $Ba_7S_{0.504}Se_{0.496}(VS_3O)_2((S_{0.467}Se_{0.533})_2)_3$, $Ba_7S_{0.21}Se_{0.79}(VS_3O)_2((S_{0.157}Se_{0.843})_2)_3$, and $Ba_7S_{0.0972}Se_{0.9028}(VS_3O)_2((S_{0.125}Se_{0.875})_2)_3$.

They may be named in the text, respectively, as phase 1, phase 2, phase 3, and phase 4 (with increased selenide content from phase 1 → 4) for clarity.

Structure Analysis of the Selenide Derivatives

The refinement details, structural parameters, and the main geometrical features are gathered in Tables 1−5. Figure 3 shows the regular increase of the unit cell parameters upon increasing selenide in the structure. The parameters α and δ define the substitution ratio by selenide in the $Q_{isolated}$ site and in the (Q_2) pair, respectively (Table 1). Clearly, both anionic entities are impacted in more or less similar proportions upon increased selenide incorporation. For phase 2, $Q_{isolated}$ is a bit more substituted. For phase 3, α and δ are very similar, and for phase 4, (Q_2) is slightly more substituted. Thus, for a lower selenide global content, $Q_{isolated}$ is favored, and then, the (Q_2) sites take over progressively upon increasing selenide content for phases 3 and 4. Having said that, both entities are filled in significant amounts at all ratios investigated here. For (Q_2), the distinct crystallographic sites for each anion involved in the pair show a very close selenide ratio; thus, in the final refinement, they were constrained equal, which did not alter the quality of the refinement and is consistent with the occurrence of either S_2 or Se_2 pairs. We note that for phase 4

with the greater selenide content, the two (Q_2) sites' occupancies show a moderate divergence when not constrained equal. This can also be related to the evolution of the refinements. For phase 1 → 3, the overall quality of the refinements is very high and the reliability factors are excellent. For phase 4, a careful analysis of the precession images from the single-crystal XRD data shows the appearance of few low-intensity extra spots (Figure S2) compared to the other phases, which we could attribute to an additional domain. A good-quality refinement could be reached after taking into account a twin domain that we found in the proportion 5.1%. Then, a careful comparison of the selenides with the parent sulfide phase shows the opposite orientation of entities in the (ab) plane within the unit cell although the structures seem identical at first sight. This is detailed in Figure S1 and is easily noticed with the Wickoff position of one of the Ba atoms, which is 2d in the sulfide and 2c in the selenides.

More into details of the three selenide derivatives $Ba_7S_{0.504}Se_{0.496}(VS_3O)_2((S_{0.467}Se_{0.533})_2)_3$, $Ba_7S_{0.21}Se_{0.79}(VS_3O)_2((S_{0.157}Se_{0.843})_2)_3$, and $Ba_7S_{0.0972}Se_{0.9028}(VS_3O)_2((S_{0.125}Se_{0.875})_2)_3$, we found the distance Q2−Q3 between 2.325(2) and 2.385(3) Å lower than that found in $Ba_3Ta_2Se_9$ with $d_{Se-Se}= 2.50$ Å[35] and in $Sr_4Sn_2Se_9$ and $Sr_4Sn_2Se_{10}$ with 2.459 and 2.462 Å, respectively,[36] also larger than that for the oxysulfide parent compound $Ba_7S(VO_3S)_2(S_2)_3$ for which $d_{S-S} = 2.122$ Å. The distances between the selenide derivatives are consistent with the mixing of the two types of pairs (S_2) and (Se_2) and depend on the selenide content. The large cation Ba1 with highly distorted environments is coordinated to four anionic species O^{2-}, $(Se/S)_2^{2-}$, $(Se/S)^{2-}$, and S^{2-} with one characteristic Ba−O1 distance, which is almost constant (in the range 2.783(2)−2.789(1) Å) for all compounds (Figure 2b). The isolated chalcogenide anion $(Se1/S1)^{2-}$ is coordinated to six Ba^{2+} cations to form the octahedron $(Se1/S1)Ba_6$ with $d_{Ba1-(Se1/S1)}$ from 3.331(1) to
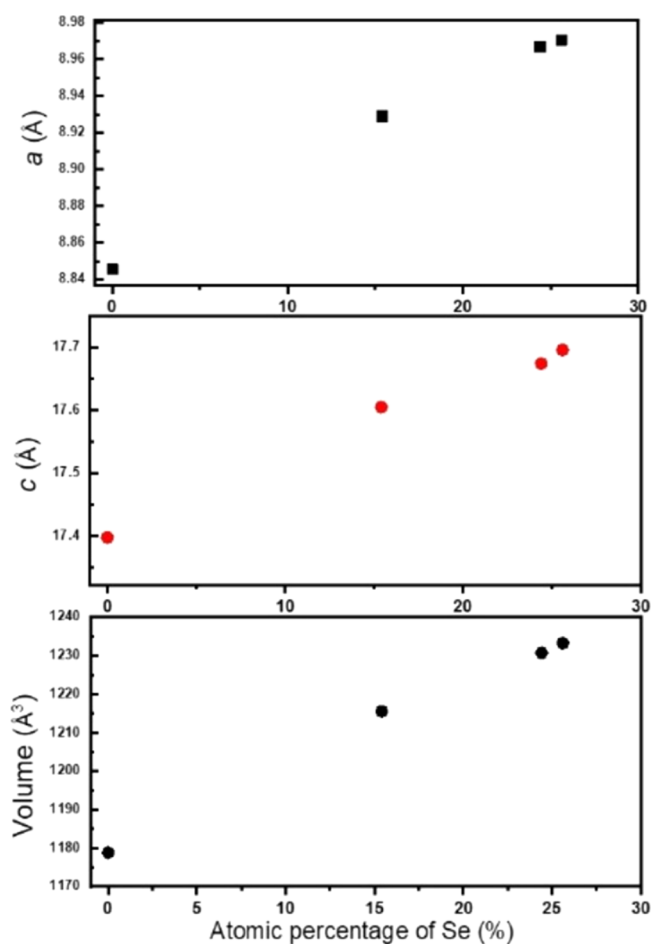
Figure 3. Unit cell parameters (*a* and *c*) and cell volume progress (from the single crystal) while the Se percentage increases. The volume and the unit cell parameters increase smoothly with the Se content (atomic percentage of Se in the phases).

3.340(1) Å in the range reported for $Ba_7Sn_3Se_{13}$[37] (d_{Se-Ba} ~ 3.183 to 3.761 Å); see Figure 2c.

Polycrystalline Phase Analysis

As depicted in Figure 4, the title phases are formed with high purity. The minor impurity $Ba_6(VO_2S_2)_2(VS_3O)(VS_4)$ was found in phase 1. Therefore, a multiphase Rietveld refinement using FullProf[38] based on the single-crystal structural model was carried out and led to very good reliability factors as shown in Figure 4 with *a* = 8.8483(1) Å and *b* = 17.4047(2) Å in the space group $P6_3/m$. The latter are very close to the one determined based on a single crystal. Rietveld quantification indicates the ratio 0.888/0.112 for the title phase Ba_7S-$(VOS_3)_2(S_2)_3$/impurity. For the Se derivatives, the profile refinement led to the unit cell parameters *a* = 8.9234(1) Å and *b* = 17.5972(2) Å for phase 2, *a* = 8.9688(1) Å and *b* = 17.6818(2) Å for phase 3, and *a* = 8.9847(1) Å and *b* = 17.7086(2) Å for phase 4. For all phases, the unit cell parameters are consistent with the single crystal, which evidence the fact that the single-crystal compositions are close to the powder and nominal compositions. For all phases, the Rietveld refinement was then carried out using the corresponding single-crystal structure, which led to very good-quality refinements. Traces of impurity $Ba_6(VO_2S_2)_2(VS_3O)(VS_4)$ might be present in the selenide derivatives, which are barely visible from the background and

thus not taken into account for the refinements. We note that the compositions refined from single crystals for phase 2 and phase 4 have discrepancies with the nominal composition concerning the S/Se ratio, which are more significant. This might happen during the crystal growth process. Regarding the level of discrepancy and since the crystals found in the powder preparation are in a minor amount, the impact on the XRD powder pattern is difficult to observe as it would induce very small quantities of impurities.

Optical Measurements

UV−visible diffuse-reflectance analysis of the polycrystalline phases (1 → 4) is represented in Figure 5. A Kubelka−Munk transformation[39] was applied to the measured diffuse-reflectance (*R*) spectra using the function $F(R) = (1 − R)^2/2R$. Then, a Tauc plot[40,41] was used to determine the optical band gap E_g using the equation $[F(R)h\nu]^{1/n} = k(h\nu − E_g)$, where $h\nu$ is the photon energy, *k* is an energy-independent constant, E_g is the optical band gap, and *n* is an exponent related to the type of transition. Assuming an indirect transition (exponent *n* = 2), the plot of $[F(R)h\nu]^2$ versus $h\nu$ is allowed, after drawing a tangent line at the inflection point, to determine the band gap as shown in Figure 4. This is consistent with the observed dark color of the crystals and powders. Figure S3 shows the band-gap evolution as a function of the Se content, and although in a narrow range, it decreases when the Se content increases as expected.

DFT Calculations Using the Meta-GGA SCAN Functional

To better understand the local geometry of selective and ordered substitution, and by consequence the origin of the experimental disorder, DFT calculations were carried out on four hypothetical phases: $Ba_7S(VS_3O)_2(S_2)_3$, Ba_7Se-$(VS_3O)_2(Se_2)_3$, $Ba_7S(VS_3O)_2(Se_2)$-following selenide-deriv, and $Ba_7Se(VS_3O)_2(S_2)_3$. To allow straightforward comparison, the models were built starting from the oxysulfide unit cell in which we apply a selective substitution at the disulfide pair sites or the isolated sulfide site or both, yielding the above-mentioned models, which were fully relaxed (Tables S5−S8). The unit cells with the band structures are shown in Figure 6 and focus on the region around the Fermi level at the top of the valence band (VB) and the bottom of the conduction band (CB). The main crystallochemical information of the optimized geometries listed in Table 6 show constant distances within VOS_3 tetrahedra and Q−Q bonds considering all hypothetical phases. It highlights the rigidity of those entities that are not disturbed by the substitutions. On the other hand, we show that the Barium environment constitutes the "flexible part" and has to absorb the chemical pressure by adjusting the Ba−O and the Ba−Q distances when the complementary layer is substituted. This adaptation does not seem to be thermodynamically favorable in our experimental conditions. Instead, the systems stabilize with concomitant incorporation of selenide in both layers to avoid interlayer mismatch and constraints.

The band structures show an indirect band gap for $Ba_7S(VS_3O)_2(S_2)_3$, $Ba_7Se(VS_3O)_2(Se_2)_3$, and Ba_7S-$(VS_3O)_2(Se_2)_3$, and then, a transition to a direct band gap for $Ba_7Se(VS_3O)_2(S_2)_3$ is observed. The variation of the band-gap width is coherent (decreases with the increase of the Se/S ratio) except in the case of $Ba_7S(VS_3O)_2(Se_2)_3$ in comparison with $Ba_7Se(VS_3O)_2(Se_2)_3$, where the band gap slightly decreases by substitution of isolated Se by S. It can be explained by the positive chemical pressure induced by the
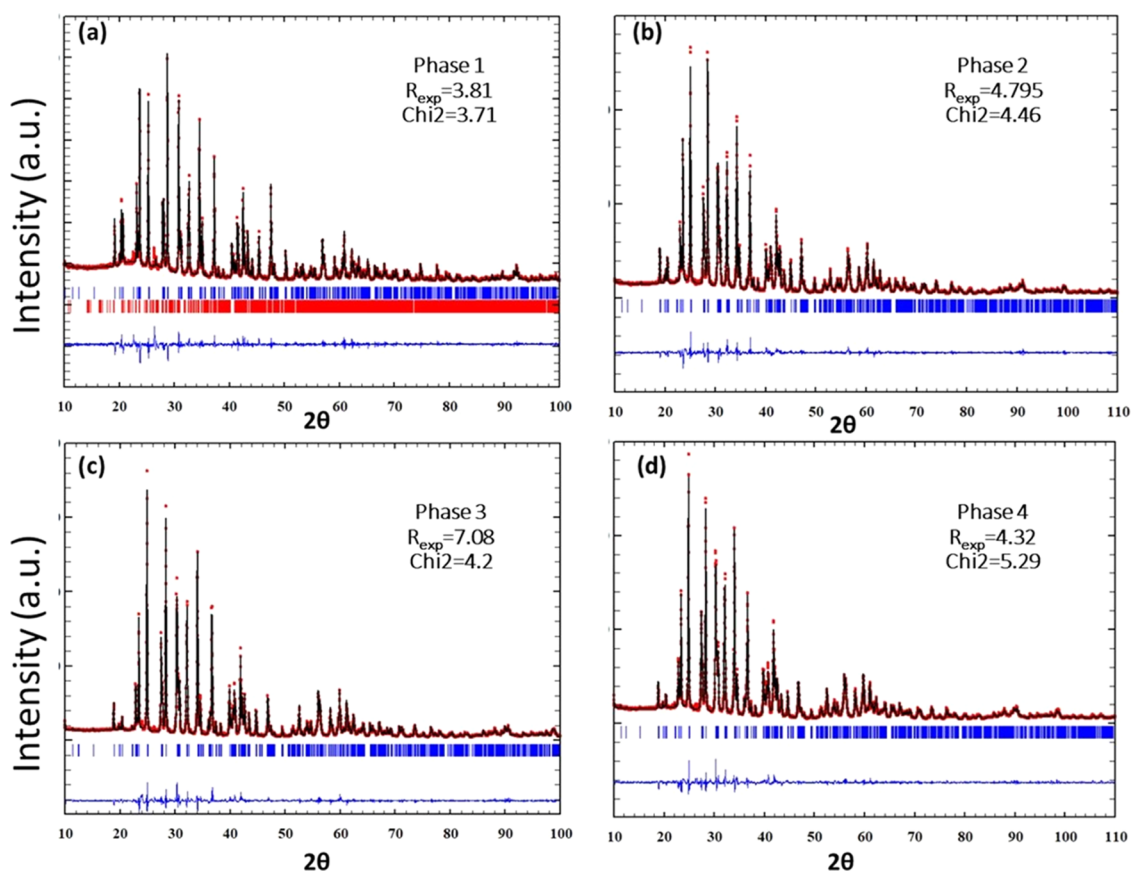
Figure 4. (a−d) Powder XRD Rietveld refinement of phases 1, 2, 3, and 4, respectively: the experimental (black) and calculated (red) patterns are superimposed; the difference curve and Bragg positions are represented in blue and green, respectively. The unit cell parameters refined in the space group $P6_3/m$ are $a = 8.8483(1)$ and $b = 17.4047(2)$ Å for phase 1; $a = 8.9234(1)$ Å and $b = 17.5972(2)$ Å for phase 2; $a = 8.9688(1)$ Å and $b = 17.6818(2)$ Å for phase 3; and $a = 8.9847(1)$ Å and $b = 17.7086(2)$ Å for phase 4.
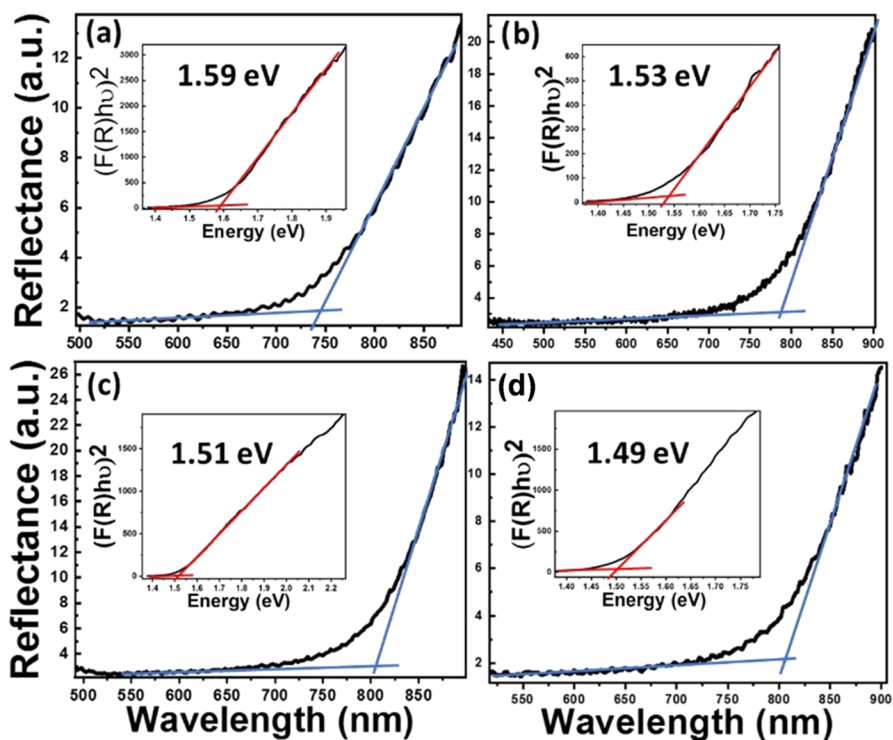
Figure 5. Diffuse-reflectance spectra of (a) phase 1, (b) phase 2, (c) phase 3, and (d) phase 4 with a Tauc plot as an inset to determine the experimental band gap.
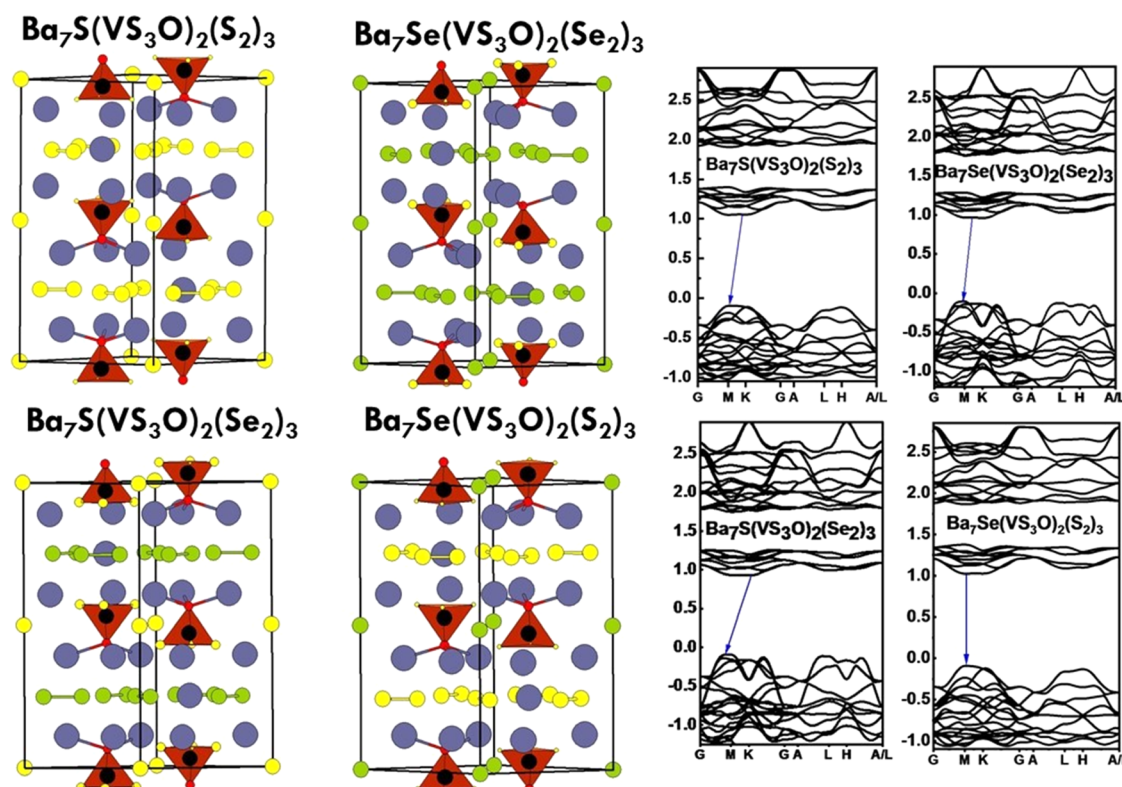
Figure 6. Unit cell of the hypothetical phases and their band structure along high symmetry points of the Brillouin zone. Ba, V, O, S, and Se are represented in purple, black, red, yellow, and green, respectively.

Table 6. Main Geometrical Information Obtained from DFT Calculations for the Hypothetical Phases

	$Ba_7S(VS_3O)_2(S_2)_3$	$Ba_7Se(VS_3O)_2(Se_2)_3$	$Ba_7S(VS_3O)_2(Se_2)_3$	$Ba_7Se(VS_3O)_2(S_2)_3$
unit cell (Å)	$a = 8.9088$, $c = 17.5491$	$a = 9.0677$, $c = 17.9483$	$a = 9.0391$, $c = 17.8805$	$a = 8.9359$, $c = 17.5970$
volume (Å³)	1206.20	1278.05	1265.20	1216.88
VO_3S (Td) distances (Å)	V−O = 1.6848	V−O = 1.6903	V−O = 1.6850	V−O = 1.6906
	V−S = 2.134	V−S = 2.1387	V−S = 2.1388	V−S = 2.1346
Ch−Ch (Å)	2.1141 (S_2)	2.4334 (Se_2)	2.4349 (Se_2)	2.1138 (S_2)
Ba−Ch$_{(isolé)}$ (Å)	3.3163	3.3798	3.3211	3.3679
Ba−Ch$_{(paire)}$ (Å)	3.2630/3.3025	3.4088/3.4547	3.4048/3.4423	3.2716/3.3134
Ba−Ch interlayer (Å)	3.7346	3.7938	3.7819	3.746
band gap (eV)	1.15 (indirect)	1.07 (indirect)	1.02 (indirect)	1.12 (direct)

smaller radius of sulfur leading to decreased Ba−Q$_{isolated}$ distances as well as closer layers. These structural changes impact the band gap toward a decrease contrarily to sulfur incorporation, and the overall effects add up and lead to the slight decrease observed.

The total density of states (DOS) of each hypothetical phase is shown in Figure 7. The contribution of each type of anionic species is also represented to compare their contribution. For $Ba_7S(VS_3O)_2(S_2)_3$, within the VS$_3$O building units, the V states lie in the CB starting from ~1.0 up to ~3 eV for the major contribution to the CBM. In the VB, the V states' contribution is found roughly in the range of −5 to −1 eV, where they are hybridized with the O 2p and S 3p states involved in the VS$_3$O building units. Owing to its more ionic bonding to vanadium and its higher electronegativity, O has a contribution of its 2p states more localized and lower in the VB (with the main large peak centered around −4.5 eV) compared to S$_{(VOS3)}$ states that are found higher in the VB mainly above −4 eV. In a previous work (ref 23), the projected DOS on distinct mixed-anion tetrahedra V(O,S)$_4$ as found in $Ba_6(VO_2S_2)_2(VS_3O)(VS_4)$

allowed one to illustrate the evolution of their contributions higher in the VB when increasing the S content (from $VO_3S \rightarrow VS_4$), thus contributing to decreasing the band gap.

The disulfide pairs and the isolated S$^{2−}$ contribute in a similar way as they are both found just below the Fermi level, above the broader S$^{2−}$ states involved in the VOS$_3$ tetrahedra, with less localized states in the former due to the S−S covalent bonding. Regarding the electronic structure description and the crystallochemical situation of each anionic species, the title phase may be decomposed as a combination of the structural entities $(Ba_7)^{14+}(S^{2−})(S_2)_3^{6−}((VS_3O)_2)^{6−}$. A similar analysis can be made for all hypothetical phases.

Considering all hypothetical phases, the dichalcogenide pairs and the isolated chalcogenide states lie in a very close energy range (without interacting). However, the $(Q)_2$ pairs dominate except in the case of $Ba_7Se(VS_3O)_2(S_2)_3$, where the isolated Se is highly present at the top of the VBM.
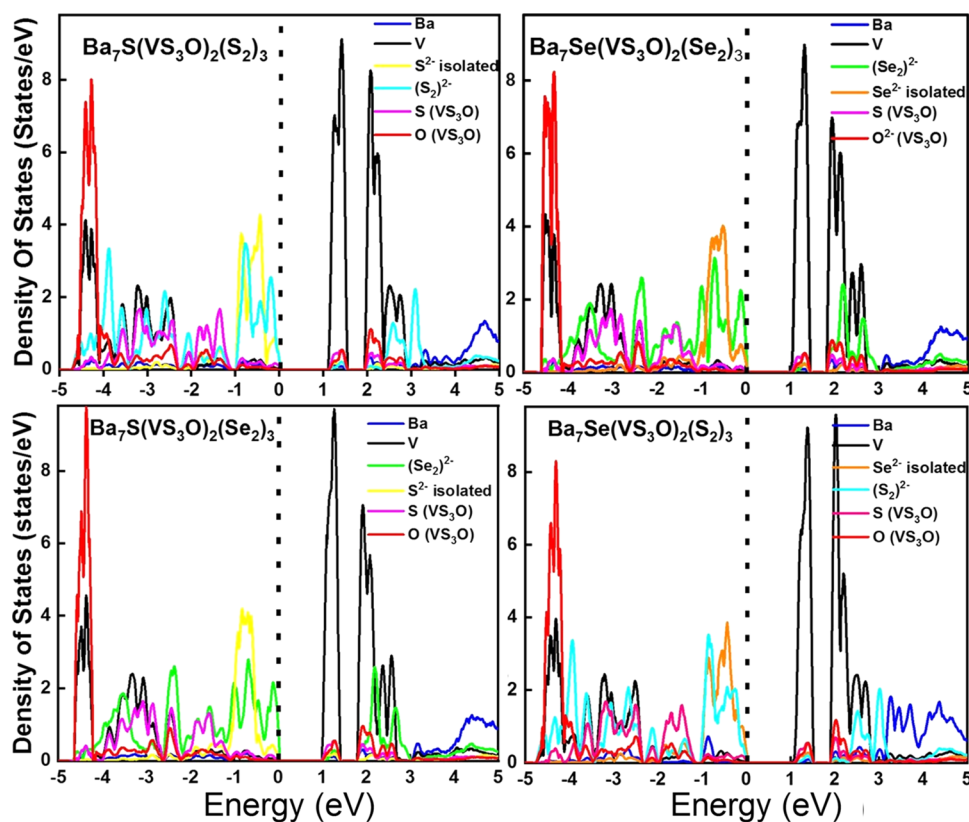
Figure 7. Projected density of states of the four hypothetical phases. The distinct contribution of each species is given: Ba; V, sulfur, and oxygen involved in a tetrahedral (VS$_3$O); Q (Q = S, Se) in isolated sites; and Q involved in a pair Q$_2$.

Table 7. Net Atomic Bader Charges for the Four Hypothetical Phases

net atomic Bader charges	Ba$_7$S(VS$_3$O)$_2$(S$_2$)$_3$	Ba$_7$Se(VS$_3$O)$_2$(Se$_2$)$_3$	Ba$_7$S(VS$_3$O)$_2$(Se$_2$)$_3$	Ba$_7$Se(VS$_3$O)$_2$(S$_2$)$_3$
Ba1	+1.49	+1.472	+1.476	+1.485
Ba2	+1.46	+1.442	+1.441	+1.464
V	+1.584	+1.588	+1.585	+1.583
S$_{(VO_3S)}$	−0.994	−1.007	−1.008	−0.994
Ch$_{(isolated)}$	−1.319	−1.270	−1.338	−1.248
Ch1−Ch2$_{(pair)}$	−0.752/−0.662	−0.701/−0.662	−0.700/−0.655	−0.695/−0.726
O	−1.019	−1.031	−1.014	−1.031

Bader Charge Analysis

Bader charge analysis[42] was carried out from the DFT calculated electronic structure based on the meta-GGA SCAN functional[30] that allows in particular a 20−50% band gap improvement[43] compared to the GGA functionals known to underestimate them and with no major additional computational cost compared to the costly hybrid functionals. We expect to obtain values closer to experience although here we focus on the comparison from one composition to another. Table 7 gathers the band-gap values and the net atomic Bader charges on the different types of atoms. For the Bader charges also, the comparative study is relevant, while the absolute values are not to be taken literally. We found Bader net charges consistent with those reported for comparable entities in the literature. For instance, (Se) values from a dichalcogenide pair are in the same range as reported in Sn(Se$_2$);[44] S^{2-} presents comparable values to that in FePS$_3$.[45] On the other hand, LiMnVO$_4$ exhibits for V^{5+} a slightly higher value of +1.80,[46] which is consistent with the fact that V^{5+} in our VO$_3$S thiovanadate involves one more covalent V−S bond

contribution compared to the vanadate VO$_4$. The Bader charges might be another way to probe the impact of substituting one layer only, for instance, we compare Ba$_7$S(VS$_3$O)$_2$(S$_2$)$_3$ with Ba$_7$S(VS$_3$O)$_2$(Se$_2$)$_3$ and Ba$_7$Se-(VS$_3$O)$_2$(Se$_2$)$_3$ with Ba$_7$Se(VS$_3$O)$_2$(S$_2$)$_3$.

Overall, the changes are rather small, thus making difficult any interpretation; however, some species show a significant evolution, which may be analyzed as follows. Overall, variations of the atomic net Bader charge of ions involved in the VO$_3$S entities show less significant evolution in accordance with their rigid geometry through compositional change. Considering models with a fixed thiovanadate layer and containing S$_{(isolated)}$$^{2-}$, a slight augmentation (0.019) of the S$_{(isolated)}$$^{2-}$ net Bader charge is observed when the nature of the complementary layer goes from (S$_2$) to (Se$_2$) pairs. This is due to the negative chemical pressure induced by the complementary layer, (S$_2$) → (Se$_2$), which enhances the ionic character of the Ba−S$_{(isolated)}$ bonds. Oppositely, for Se$_{(isolated)}$ in fixed thiovanadates layers, a decrease (0.022) is observed due to the positive chemical pressure from (Se$_2$) → (S$_2$) in the complementary layer yielding more covalent Ba−

$Se_{(isolated)}$ bonds. A similar analysis can be made for $Se_{(Se2)}$, where the net Bader charge decreases through exchange of $Se_{isolated}$ by S in the complementary layer, which induces a positive chemical pressure that should enhance covalent bonding. However, the counterintuitive $S_{(S2)}$ net Bader charge decrease (more covalent bonding) through exchange of $S_{isolated}$ by $Se_{isolated}$ (negative chemical pressure) in the complementary layer indicates a more complicated scenario, which may be related to the band-gap evolution described above for this case.

CONCLUSIONS

A new series of thiovanadate polychalcogenide phases $Ba_7V_2S_{13}O_2$ and three selenide derivatives $Ba_7V_2O_2S_{9.304}Se_{3.696}$, $Ba_7V_2O_2S_{7.15}Se_{5.85}$, and $Ba_7V_2O_2S_{6.85}Se_{6.15}$ were elaborated, and their structures were solved in the space group $P6_3/m$ (176). They represent original and complex multianionic manipulation examples. $Ba_7V_2S_{13}O_2$ is the sixth member in the quaternary system Ba−V−S−O (the second with disulfide pairs), while the three selenide derivatives are the first ones in the system Ba−V−Se−S−O. These phases exhibit mixed-anion building units VOS_3, isolated Q^{2-} (Q = S, Se) sites (present in one layer), and isolated dichalcogenide pairs Q_2 (in the second layer). We show that all attempts of a selective substitution of sulfur by selenide in our synthetic conditions led to concomitant incorporation of Se in both the isolated Q and Q_2 pairs sites with mixed S/Se occupancy. It indicates that two types of pairs S_2 and Se_2 are present in the selenide derivatives, which can be monitored by the mean Q−Q distance refined and which evolve with respect to the substitution level. Our meta-GGA DFT calculations, including Bader charge analysis, on the sulfide and three ordered selenide derivatives showed that the substitution in one layer only leads to local structural variations that are absorbed by the Ba sublattice, while VO_3S and Q_2 pairs remain rigid. This might explain the experimental disorder to avoid such constraints. Rationalization of the structure with respect to the electronic structure is interesting for designing new phases using such mixed-anion building blocks and/or dichalcogenide pairs. In particular, band-gap engineering through mastered approaches is important for a variety of properties.

ASSOCIATED CONTENT

Data Availability Statement

The data underlying this study are available in the published article and its Supporting Information.

ⓈⒾ Supporting Information

The Supporting Information is available free of charge at https://pubs.acs.org/doi/10.1021/acsorginorgau.3c00006.

> Data collection and refinement details of $Ba_7V_2O_2S_{13}$ synthesized at high pressures with a description of the synthesis (Table S1 and text below); atomic positions, isotropic thermal displacement, anisotropic thermal parameters, and main distances for $Ba_7V_2O_2S_{13}$ obtained with the high-pressure technique (Tables S2−S4); optimized structures information in Tables S5−S8; comparison between the oxysulfide phase and one of the selenide derivatives (Figure S1); precessions images (Figure S2); and band gap as a function of the selenide content (Figure S3) (PDF)

■ AUTHOR INFORMATION

Corresponding Author

Houria Kabbour − *Univ. Lille, CNRS, Centrale Lille, ENSCL, Univ. Artois, UMR 8181-UCCS-Unité de Catalyse et Chimie du Solide, F-59000 Lille, France;* ⓞ orcid.org/0000-0002-9081-3261; Email: houria.kabbour@univ-lille.fr

Authors

Batoul Almoussawi − *Univ. Lille, CNRS, Centrale Lille, ENSCL, Univ. Artois, UMR 8181-UCCS-Unité de Catalyse et Chimie du Solide, F-59000 Lille, France*

Hiroshi Kageyama − *Department of Energy and Hydrocarbon Chemistry, Graduate School of Engineering, Kyoto University, Nishikyo-ku, Kyoto 615-8510, Japan;* ⓞ orcid.org/0000-0002-3911-9864

Pascal Roussel − *Univ. Lille, CNRS, Centrale Lille, ENSCL, Univ. Artois, UMR 8181-UCCS-Unité de Catalyse et Chimie du Solide, F-59000 Lille, France;* ⓞ orcid.org/0000-0001-7243-7293

Complete contact information is available at:
https://pubs.acs.org/10.1021/acsorginorgau.3c00006

Author Contributions

CRediT: **Batoul Almoussawi** conceptualization (supporting), formal analysis (equal), investigation (lead), methodology (equal), project administration (equal), writing-original draft (lead), writing-review & editing (supporting); **Hiroshi Kageyama** conceptualization (supporting), funding acquisition (supporting), investigation (supporting), methodology (supporting), supervision (supporting), validation (equal), writing-review & editing (supporting); **Pascal Roussel** formal analysis (supporting), methodology (supporting), validation (supporting), writing-review & editing (supporting); **Houria Kabbour** conceptualization (lead), formal analysis (equal), funding acquisition (lead), investigation (supporting), methodology (equal), project administration (equal), supervision (lead), validation (equal), writing-original draft (supporting), writing-review & editing (lead).

Notes

The authors declare no competing financial interest.

■ REFERENCES

(1) Kageyama, H.; Hayashi, K.; Maeda, K.; Attfield, J. P.; Hiroi, Z.; Rondinelli, J. M.; Poeppelmeier, K. R. Expanding Frontiers in Materials Chemistry and Physics with Multiple Anions. *Nat. Commun.* **2018**, *9*, No. 772.

(2) Nayak, S.; Nagaraja, K. K. High Anisotropy in the Electronic and Thermoelectric Properties of Layered Oxysulfides: A Case Study of LaOPbBiS$_3$. *J. Alloys Compd.* **2020**, *814*, No. 152137.

(3) Labégorre, J.-B.; Al Rahal Al Orabi, R.; Virfeu, A.; Gamon, J.; Barboux, P.; Pautrot-d'Alençon, L.; Le Mercier, T.; Berthebaud, D.; Maignan, A.; Guilmeau, E. Electronic Band Structure Engineering and Enhanced Thermoelectric Transport Properties in Pb-Doped BiCuOS Oxysulfide. *Chem. Mater.* **2018**, *30*, 1085−1094.

(4) Wang, Q.; Nakabayashi, M.; Hisatomi, T.; Sun, S.; Akiyama, S.; Wang, Z.; Pan, Z.; Xiao, X.; Watanabe, T.; Yamada, T.; et al. Oxysulfide Photocatalyst for Visible-Light-Driven Overall Water Splitting. *Nat. Mater.* **2019**, *18*, 827−832.

(5) Kabbour, H.; Sayede, A.; Saitzek, S.; Lefèvre, G.; Cario, L.; Trentesaux, M.; Roussel, P. Structure of the Water-Splitting Photocatalyst Oxysulfide α-LaOInS$_2$ and Ab Initio Prediction of New Polymorphs. *Chem. Commun.* **2020**, *56*, 1645−1648.

(6) Luu, S. D. N.; Vaqueiro, P. Layered Oxychalcogenides: Structural Chemistry and Thermoelectric Properties. *J. Materiomics* **2016**, *2*, 131−140.

(7) Blandy, J. N.; Liu, S.; Smura, C. F.; Cassidy, S. J.; Woodruff, D. N.; McGrady, J. E.; Clarke, S. J. Synthesis, Structure, and Properties of the Layered Oxide Chalcogenides Sr$_2$CuO$_2$Cu$_2$S$_2$ and Sr$_2$CuO$_2$Cu$_2$Se$_2$. *Inorg. Chem.* **2018**, *57*, 15379−15388.

(8) Evans, J. S. O.; Brogden, E. B.; Thompson, A. L.; Cordiner, R. L. Synthesis and Characterisation of the New Oxyselenide Bi$_2$YO$_4$Cu$_2$Se$_2$. *Chem. Commun.* **2002**, *8*, 912−913.

(9) Deguchi, K.; Mizuguchi, Y.; Demura, S.; Hara, H.; Watanabe, T.; Denholme, S. J.; Fujioka, M.; Okazaki, H.; Ozaki, T.; Takeya, H.; et al. Evolution of Superconductivity in LaO$_{1-x}$F$_x$BiS$_2$ Prepared by High-Pressure Technique. *Europhys. Lett.* **2013**, *101*, No. 17004.

(10) Sasaki, S.; Lesault, M.; Grange, E.; Janod, E.; Corraze, B.; Cadars, S.; Caldes, M. T.; Guillot-Deudon, C.; Jobic, S.; Cario, L. Unexplored Reactivity of (Sn)$^{2-}$ Oligomers with Transition Metals in Low-Temperature Solid-State Reactions. *Chem. Commun.* **2019**, *55*, 6189−6192.

(11) Nowack, E.; Schwarzenbach, D.; Hahn, T. Charge Densities in CoS$_2$ and NiS$_2$ (Pyrite Structure). *Acta Crystallogr., Sect. B* **1991**, *47*, 650−659.

(12) Adachi, K.; Matsui, M.; Kimura, F.; Omata, Y. Electron Correlation and Band Width of Dγ 1 Pyrite Compounds. *J. Phys. Soc. Jpn.* **1980**, *49*, 1629−1630.

(13) Guo, Y.; Shang, C.; Wang, E. An Efficient CoS$_2$/CoSe$_2$ Hybrid Catalyst for Electrocatalytic Hydrogen Evolution. *J. Mater. Chem. A* **2017**, *5*, 2504−2507.

(14) Hao, J.; Xu, X.; You, H.; Min, H.; Liu, X.; Yang, H. The Free-Standing Cathode Fabricated with Nano-CoSe$_2$ Embedded in Mesoporous Carbon Nanosheets towards High Performance Li/SeS$_2$ Batteries. *Chem. Eng. J.* **2021**, *418*, No. 129475.

(15) Leriche, R. T.; Palacio-Morales, A.; Campetella, M.; Tresca, C.; Sasaki, S.; Brun, C.; Debontridder, F.; David, P.; Arfaoui, I.; Šofranko, O.; et al. Misfit Layer Compounds: A Platform for Heavily Doped 2D Transition Metal Dichalcogenides. *Adv. Funct. Mater.* **2021**, *31*, No. 2007706.

(16) Maier, S.; Ohno, S.; Yu, G.; Kang, S. D.; Chasapis, T. C.; Ha, V. A.; Miller, S. A.; Berthebaud, D.; Kanatzidis, M. G.; Rignanese, G.-M.; et al. Resonant Bonding, Multiband Thermoelectric Transport, and Native Defects in n-Type BaBiTe$_{3-x}$Se$_x$ (x = 0, 0.05, and 0.1). *Chem. Mater.* **2018**, *30*, 174−184.

(17) Patschke, R.; Zhang, X.; Singh, D.; Schindler, J.; Kannewurf, C. R.; Lowhorn, N.; Tritt, T.; Nolas, G. S.; Kanatzidis, M. G. Thermoelectric Properties and Electronic Structure of the Cage Compounds A$_2$BaCu$_8$Te$_{10}$ (A = K, Rb, Cs): Systems with Low Thermal Conductivity. *Chem. Mater.* **2001**, *13*, 613−621.

(18) Kabbour, H.; Sayede, A.; Saitzek, S.; Lefèvre, G.; Cario, L.; Trentesaux, M.; Roussel, P. Structure of the Water-Splitting Photocatalyst Oxysulfide α-LaOInS$_2$ and: Ab Initio Prediction of New Polymorphs. *Chem. Commun.* **2020**, *56*, 1645−1648.

(19) Sasaki, S.; Caldes, M. T.; Guillot-Deudon, C.; Braems, I.; Steciuk, G.; Palatinus, L.; Gautron, E.; Frapper, G.; Janod, E.; Corraze, B.; et al. Design of Metastable Oxychalcogenide Phases by Topochemical (de)Intercalation of Sulfur in La$_2$O$_2$S$_2$. *Nat. Commun.* **2021**, *12*, No. 3605.

(20) Almoussawi, B.; Huvé, M.; Dupray, V.; Clevers, S.; Duffort, V.; Mentré, O.; Roussel, P.; Arevalo-Lopez, A. M.; Kabbour, H. Oxysulfide Ba$_5$(VO$_2$S$_2$)$_2$(S$_2$)$_2$ Combining Disulfide Channels and Mixed-Anion Tetrahedra and Its Third-Harmonic-Generation Properties. *Inorg. Chem.* **2020**, *59*, 5907−5917.

(21) Litteer, J. B.; Fettinger, J. C.; Eichhorn, B. W. Ba$_6$V$_4$O$_5$S$_{11}$. *Acta Crystallogr., Sect. C* **1997**, *53*, 163−165.

(22) Hopkins, E. J.; Prots, Y.; Burkhardt, U.; Watier, Y.; Hu, Z.; Kuo, C.-Y.; Chiang, J.-C.; Pi, T.-W.; Tanaka, A.; Tjeng, L. H.; Valldor, M. Ba$_3$V$_2$S$_4$O$_3$: A Mott Insulating Frustrated Quasi-One-Dimensional S =1 Magnet. *Chem. − Eur. J.* **2015**, *21*, 7938−7943.

(23) Jenks, J. M.; Hoggins, J. T.; Rendon-DiazMiron, L. E.; Cohen, S.; Steinfink, H. Octahedrally Coordinated Iron in the Barium-Iron-Sulfur System: Ba$_9$Fe$_3$S$_{11}$(S$_2$)$_2$, a High-Pressure Polymorph of Ba$_3$FeS$_5$. *Inorg. Chem.* **1978**, *17*, 1773−1775.

(24) Nicoud, S.; Mentré, O.; Kabbour, H. The Ba$_{10}$S(VO$_3$S)$_6$ Oxysulfide: One-Dimensional Structure and Mixed Anion Chemical Bonding. *Inorg. Chem.* **2019**, *58*, 1349−1357.

(25) Schnabel, S.; Röhr, C. Gemischte Thio/Oxo-Orthovanadate Na$_3$[VS$_x$O$_4$$_{−x}$] (x = 2, 3): Darstellung − Strukturen − Eigenschaften/ Mixed Thio/Oxo Orthovanadates Na$_3$[VS$_x$O$_{4-x}$] (x = 2, 3): Synthesis − Crystal Structures − Properties. *Z. Naturforsch. B* **2005**, *60*, 479−490.

(26) Blöchl, P. E. Projector Augmented-Wave Method. *Phys. Rev. B* **1994**, *50*, 17953−17979.

(27) Kresse, G.; Joubert, D. From Ultrasoft Pseudopotentials to the Projector Augmented-Wave Method. *Phys. Rev. B* **1999**, *59*, 1758−1775.

(28) Kresse, G.; Furthmüller, J. Efficient iterative schemes for ab initio total-energy calculations using a plane-wave basis set. *Phys. Rev. B* **1996**, *54*, 11169.

(29) Tao, J.; Perdew, J. P.; Staroverov, V. N.; Scuseria, G. E. Climbing the Density Functional Ladder: Nonempirical Meta–Generalized Gradient Approximation Designed for Molecules and Solids. *Phys. Rev. Lett.* **2003**, *91*, No. 146401.

(30) Yang, Z.-h.; Peng, H.; Sun, J.; Perdew, J. P. More Realistic Band Gaps from Meta-Generalized Gradient Approximations: Only in a Generalized Kohn-Sham Scheme. *Phys. Rev. B* **2016**, *93*, No. 205205.

(31) Petříček, V.; Dušek, M.; Palatinus, L. Crystallographic Computing System JANA2006: General Features. *Z. Kristallogr. − Cryst. Mater.* **2014**, *229*, 345−352.

(32) van der Lee, A. Charge Flipping for Routine Structure Solution. *J. Appl. Crystallogr.* **2013**, *46*, 1306−1315.

(33) Almoussawi, B.; Tomohiri, H.; Kageyama, H.; Kabbour, H. High Pressure Synthesis of the Spin Chain Sulfide Ba$_9$V$_3$S$_{11}$(S$_2$)$_2$. *Eur. J. Inorg. Chem.* **2021**, *2021*, 1271−1277.

(34) Schnabel, S.; Röhr, C. Potassium Thio/Oxo-Vanadates(V) K$_3$[VS$_x$O$_{4-x}$] (x = 1-4) and Na$_3$[VSO$_3$]: Synthesis, Structural Chemistry, Properties. *Z. Naturforsch. B* **2008**, *63*, 819−833.

(35) Chung, M.-Y.; Lee, C.-S. Ba$_3$TM$_2$Se$_9$ (TM: Nb, Ta): Synthesis and Characterization of New Polyselenides. *Inorg. Chem.* **2014**, *53*, 80−84.

(36) Pocha, R.; Johrendt, D. Crystal Structures of Sr$_4$Sn$_2$Se$_9$ and Sr$_4$Sn$_2$Se$_{10}$ and the Oxidation State of Tin in an Unusual Geometry. *Inorg. Chem.* **2004**, *43*, 6830−6837.

(37) Assoud, A.; Kleinke, H. Unique Barium Selenostannate—Selenide: Ba$_7$Sn$_3$Se$_{13}$ (and Its Variants Ba$_7$Sn$_3$Se$_{13-\Delta}$Te$_\delta$) with SnSe$_4$

Tetrahedra and Isolated Se Anions. *Chem. Mater.* **2005**, *17*, 4509−4513.

(38) Rodriguez-Carvajal, J. Recent Developments of the Program FULLPROF, Commission on Powder Diffraction. *IUCr Newsl.* **2001**, *26*, 12−19.

(39) Tauc, J.; Grigorovici, R.; Vancu, A. Optical Properties and Electronic Structure of Amorphous Germanium. *Phys. Status Solidi B* **1966**, *15*, 627−637.

(40) Kubelka, P.; Munk, F. Ein Beitrag Zur Optik Der Farbanstriche. Zeitschrift Für Technische Physik. *Tech. Phys.* **1931**, *12*, 593−601.

(41) Wendlandt, W.; Hecht, H. G. *Reflectance Spectroscopy*; Interscience: New York, 1966.

(42) Yu, M.; Trinkle, D. R. Accurate and Efficient Algorithm for Bader Charge Integration. *J. Chem. Phys.* **2011**, *134*, No. 064111.

(43) Sun, J.; Remsing, R. C.; Zhang, Y.; Sun, Z.; Ruzsinszky, A.; Peng, H.; Yang, Z.; Paul, A.; Waghmare, U.; Wu, X.; et al. Accurate First-Principles Structures and Energies of Diversely Bonded Systems from an Efficient Density Functional. *Nat. Chem.* **2016**, *8*, 831−836.

(44) Choe, J. S.; Lee, C.; Kim, M. J.; Lee, G.-G.; Shim, J.-H.; Lim, Y. S. Bader Net Charge Analysis on Doping Effects of Sb in $SnSe_2$ and Related Charge Transport Properties. *J. Appl. Phys.* **2020**, *127*, No. 185706.

(45) Sen, P.; Chouhan, R. K. Electronic Structure of MPX_3 Trichalcogenide Monolayers in Density Functional Theory: A Case Study with Four Compounds (M = Mn, Fe; X = S, Se). *Electron. Struct.* **2020**, *2*, No. 025003.

(46) Clemens, O.; Haberkorn, R.; Kohlmann, H.; Springborg, M.; Beck, H. P. Synthesis and Characterization of the New Mixed Valent Compound Mn_5VO_8. *Z. Anorg. Allg. Chem.* **2012**, *638*, 1134−1140.